

# Sequential tilting 4D-STEM for improved momentum-resolved STEM field mapping

Christoph Flathmann<sup>\*1,2,3</sup>, Ulrich Ross<sup>1</sup>, Jürgen Belz<sup>4</sup>, Andreas Beyer<sup>4</sup>, Kerstin Volz<sup>4</sup>, Michael Seibt<sup>1</sup>, and Tobias Meyer<sup>†5</sup>

<sup>1</sup>4th Institute of Physics – Solids and Nanostructures,  
University of Goettingen, Friedrich-Hund-Platz 1, 37077  
Göttingen, Germany

<sup>2</sup>Research Center Future Energy Materials and Systems, Ruhr  
University Bochum, Universitätsstr. 150, 44801 Bochum,  
Germany

<sup>3</sup>Faculty of Physics and Astronomy, Ruhr University Bochum,  
Universitätsstr. 150, 44801 Bochum, Germany

<sup>4</sup>Department of Physics and Materials Science Center,  
Philipps-University Marburg, Hans-Meerwein Str. 6, 35032  
Marburg, Germany

<sup>5</sup>Institute of Materials Physics, University of Goettingen,  
Friedrich-Hund-Platz 1, 37077 Göttingen, Germany

May 29, 2025

\*Corresponding author: christoph.flathmann@ruhr-uni-bochum.de

†Corresponding author: tmeyer@uni-goettingen.de

## Abstract

Momentum-resolved scanning transmission electron microscopy (MRSTEM) is a powerful phase-contrast technique that can map lateral magnetic and electric fields ranging from the micrometer to the subatomic scale. Resolving fields ranging from a few nanometers to a few hundred nanometers, as well as across material junctions, is particularly important since these fields often determine the functional properties of devices. However, it is also challenging since they are orders of magnitude smaller than atomic electric fields. Thus, subtle changes in diffraction conditions lead to significant changes in the measured MRSTEM signal. One established approach to partially overcome this problem is precession electron diffraction, in which the incident electron beam is continuously precessed while precession-averaged diffraction patterns are acquired. Here, we present an alternative approach in which we sequentially tilt the incident electron beam and record a full diffraction pattern for each tilt and spatial position. This approach requires no hardware modification of the instrument and enables the use of arbitrary beam tilt patterns that can be optimized for specific applications. Furthermore, recording diffraction patterns for every beam tilt allows access to additional information. In this work, we use this information to create virtual large-angle convergent beam electron diffraction (vLACBED) patterns to assess MRSTEM data quality and improve field measurements by applying different data analysis methods beyond simple averaging. The presented data acquisition concept can readily be applied to other 4D-STEM applications.

# 1 Introduction

Nanometer-sized electric fields across junctions play a crucial role in electronic devices such as transistors [1], solar cells [2] or batteries [3, 4, 5], as the associated built-in potentials determine their functional properties. New concepts that improve the performance of these devices require miniaturization and increasingly complex designs. Thus, accurate measurements of the potentials on the relevant length scale of a few to about 100 nm are necessary for technological progress.

In recent years, phase-contrast transmission electron microscopy (TEM) techniques have demonstrated great potential for accomplishing this task. One such method with a long tradition of mapping potentials across junctions is off-axis electron holography [6, 7]. It has been used to study silicon p-n junctions [8, 9, 10, 11], compound semiconductors [12, 13] and quantum wells [14, 15]. However, off-axis electron holography has several drawbacks, such as the requirement of an undistorted reference wave and a limited field of view.

An alternative approach to mapping fields involves measuring the deflection of the transmitted beam in scanning transmission electron microscopy (STEM) mode. In this case, one measures the average lateral momentum transferred from the sample to the electron beam via the center of mass (COM) of the diffraction pattern [16], which is related to the lateral gradient of the projected electrostatic potential convolved with the incident probe intensity [17].

There are two methods for measuring the average momentum transfer: differential phase contrast (DPC) STEM and momentum-resolved STEM (MRSTEM). DPC uses a segmented detector to approximate the COM, allowing for the rapid acquisition of data, but is rather sensitive to the alignment of the experimental setup. Nevertheless, DPC has been used to map fields across p-n junctions and polarization fields in quantum wells [18, 19, 20, 21, 22]. With the advent of faster pixelated detectors, MRSTEM has become more common. Here, a full diffraction pattern is acquired at each scan position, enabling more robust data acquisition and post-processing than DPC. MRSTEM has been used to measure fields across p-n homojunctions with and without an applied bias, as well as potential drops across heterointerfaces [23, 24, 25, 26].

However, all the phase-contrast TEM methods have issues with quantitatively and reliably measuring extended fields. This is because fields in

the nanometer range typically have absolute values below 0.1 V/nm, which is orders of magnitude smaller than the gradients of atomic electric potentials. Thus, even small changes in the often dynamical diffraction conditions across the field of view lead to significant changes in the diffraction intensity, resulting in large and hard-to-predict signals in phase contrast TEM. This is particularly pronounced in complex samples, such as heterostructures, where strain gradients, defects, thickness variations, different lattice constants or symmetries, and local misorientation can strongly distort field measurements making it challenging to achieve accurate measurements in real devices [27, 28].

The common approach to mitigate this issue involves combining DPC or MRSTEM with precession [23, 26, 29]. In this method, the incident electron beam continuously precesses around the optical axis at a polar angle of typically around 10 mrad. The precession is hardware-synchronized with the scan, and the diffraction signal is averaged over all azimuthal angles. This incoherent average of diffraction patterns has been shown to suppress dynamical diffraction effects as compared to individual diffraction patterns [30], thus significantly improving the results of DPC and MRSTEM [26]. A comparison of the strengths and weaknesses of these convergent beam methods compared to off-axis electron holography using a plane incident wave can be found in reference [31] with the conclusion that for a proper crystal orientation a plane wave is beneficial since convergent beams more likely include incident directions with strong dynamical effects.

The approach presented here goes beyond standard precession electron diffraction and offers the possibility to reduce these dynamical diffraction effects: It sequentially records full diffraction patterns for each scan position and tilt of the incident electron beam. This provides 6-dimensional data sets, which offer more information than previous methods. It also gives us the ability to use arbitrary tilt patterns, which has been reported to be beneficial for MRSTEM [29]. The underlying principle of this sequential tilting MRSTEM is very similar to the tilt scan averaged DPC STEM presented in references [32, 33, 34, 35, 36], except that we have access to the full 6D data.

In order to experimentally verify our approach, we use sequential tilting MRSTEM on AlGaAs/GaAs heterojunctions, a well-studied model system. We use the additional information contained in the sequential tilted MRSTEM data to assess the data quality, post-process the data for different sample orientations to reduce dynamical diffraction effects, and confirm that this additional information is essential to improving the reliability and

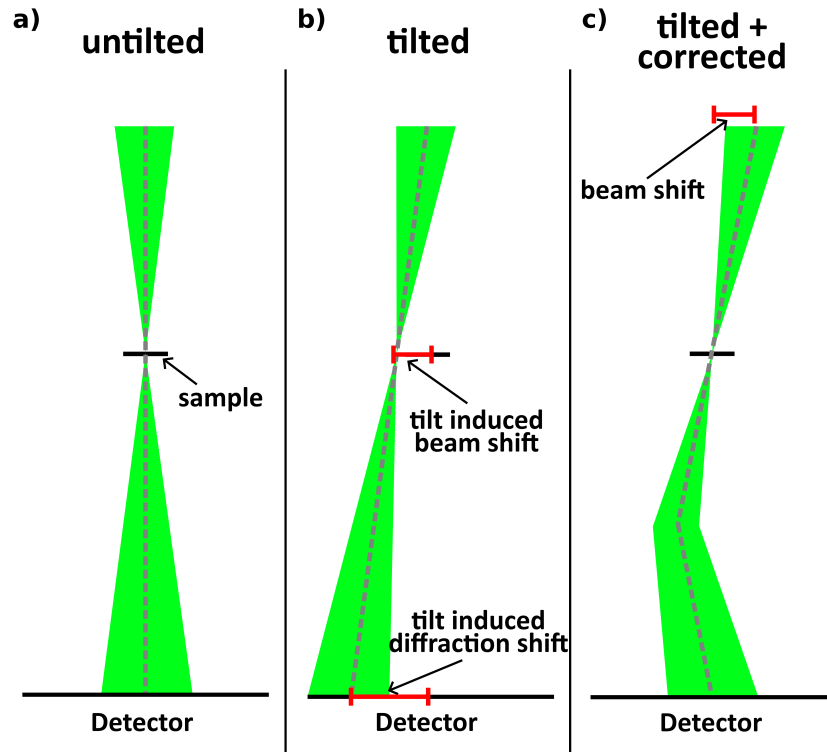


Figure 1: Beam tilt and detilt: **a)** shows the beam path without tilt. **b)** shows the beam path with tilt. **c)** shows the beam path with tilt, detilt and tilt induced shift correction. The relevant shifts are highlighted in the images.

quantifiability of MRSTEM results.

## 2 Experimental

### 2.1 Calibration procedure

To achieve precise beam tilts without hardware modifications, we implemented a custom-developed calibration and acquisition procedure. A two-step calibration process is necessary to enable the sequential tilting MRSTEM: first, calibrate the beam tilts; then, calibrate the tilt-induced beam shift. Figure 1 **a)**-**c)** shows a schematic of the beam paths for different tilt and calibration conditions, with visualizations of the relevant parameters.

The first step is to calibrate the microscope’s tilt coils via cross-correlation of diffraction patterns acquired for different beam tilts in vacuum. The calibration script accomplishes this by addressing the tilt coils with the TEM scripting interface command. However, since the input values of the command are in arbitrary units, a very small value is initially entered and gradually increased until the shift of the diffraction pattern on the detector reaches a threshold of at least 1/4 of the detector. For an known pixel spacing of the detector, the shift of the diffraction pattern provides a first quantitative beam tilt calibration which is then used as input for the fine calibration.

In the fine calibration, the beam is tilted along a circular pattern with a user-defined tilt angle (based on the estimated calibration from the previous step) and a specified number of samples. By measuring the shift of the diffraction pattern for each beam tilt, one obtains several pairs of desired and actual tilt angles of the beam. Assuming a linear relationship between the desired and actual beam tilts, the resulting system of linear equations can be solved to calibrate the beam tilt coils. This calibration process is carried out for the beam tilt coils above the sample and the detilt (diffraction shift) coils below the sample. This gives us the capability to tilt the beam above the sample while keeping the diffraction pattern stationary on the detector.

The second step is to calibrate the tilt-induced beam shift by cross-correlating STEM images. To measure this shift, the beam is tilted again along a circular pattern with a user-defined tilt angle and number of samples. This captures the tilt-induced beam shift in a similar way as the precession path segmentation, described in reference [37], used for scanning precession electron diffraction. The beam shift is measured via cross-correlation of the STEM images, and the calibration is obtained in the same manner as for the tilt coil calibration. Next, the calibration script addresses the beam shift coils of the microscope, and the corresponding beam shifts are measured via cross-correlation of the images. Similar to calibrating the tilt coils, this process involves first a coarse calibration, followed by a fine calibration. Calibrating the tilt-induced beam shift is usually more challenging than calibrating the beam tilt coils since image contrast changes with beam tilt.

## 2.2 Samples

In this study, we examine the potential distribution across heterojunctions of a nominally undoped 10-fold  $\text{Al}_{0.3}\text{Ga}_{0.7}\text{As}/\text{GaAs}$  super lattice sample. The sample was grown via metal-organic vapor phase epitaxy (MOVPE) in an

AIX 200 GFR reactor on semi insulating GaAs(001) substrate. The actual Al content was determined from high-resolution X-ray diffraction by fitting a 004  $\omega/2\theta$ -scan. It is an excellent model system because the expected MRSTEM signal results almost exclusively from a change in the mean inner potential at the interface of the two materials. Therefore, we can accurately estimate the potential profile across the AlGaAs/GaAs interface. Additionally, AlGaAs and GaAs have a negligible lattice mismatch of approximately  $\sim 0.3\%$  at room temperature, resulting in minimal strain relaxation in the sample. However, the two materials exhibit significant differences in diffraction properties due to their distinct atomic form factors ( $f_{Ga} \approx f_{As} \neq f_{Al}$ ). Therefore, we expect a substantial change in diffraction conditions across the junction but rather constant diffraction conditions on either side of the junction.

### 2.3 Equipment & Measurements

For this study, we used an image corrected Titan 80–300 G2 ETEM operated at 300 kV, equipped with a Gatan Quantum 965 ER image filter and a Gatan UltraScan 1000XP CCD camera.

We prepared cross-section TEM lamellae in [110] orientation from the sample using a standard FIB procedure in a Thermo Fisher Scientific Helios G4. The lamellae thickness was measured as 330 nm by electron energy loss spectroscopy using the log-ratio method, assuming an inelastic mean free path of 145 nm according to the method proposed by Iakoubovskii et al. [38]. Using such thick lamellae is beneficial for mapping nanometer-sized electric fields because it reduces the influence of surface effects.

All of the MRSTEM results presented in this study were acquired with a semiconvergence angle of 1 mrad, resulting in a diffraction-limited probe size of  $\sim 2$  nm, and a probe current of  $\sim 40$  pA. Sequential tilting measurements were carried out as line scans across the junction with 30 nm position averaging perpendicular to the scan direction. The beam tilt pattern was always disc-shaped and consisted of 61 beam tilts with a maximum tilt angle of 7 mrad, as shown in Figure 2 a). Diffraction patterns were acquired using a custom Gatan DigitalMicrograph<sup>®</sup> script [39] with 0.1 s exposure time, and the detector was binned to  $256 \times 256$  pixels, resulting in a pixel size of  $17.5 \mu\text{rad}$ . This produced diffraction patterns containing only the direct diffraction disc. Furthermore, the diffraction patterns were energy filtered using a 10 eV slit. To remove artifacts such as descan from the data, a

vacuum reference was taken under identical conditions for every scan.

## 3 Results & Discussion

### 3.1 Calibration quality

To get an initial idea of the tilt calibration quality, we can create a virtual large-angle convergent beam electron diffraction (vLACBED) pattern using the diffraction patterns from individual beam tilts at the same position. This is done by shifting the diffraction patterns according to their respective beam tilt angles. The vLACBED patterns for a GaAs position are shown in Figure 2 b)-d) for three different sample orientations. In particular, for the off-axis orientation, one can see that all higher-order Laue zone (HOLZ) lines (narrow features) and Bragg deficiency lines (broad features) run continuously through the vLACBED pattern, indicating that both tilt and detilt are precisely calibrated.

To analyze the tilt-induced diffraction shift remaining after calibration, we use an untilted vacuum diffraction pattern, shown in Figure 3 a), and 16 vacuum diffraction patterns tilted along a 7 mrad circular pattern. The sum of these patterns is shown in Figure 3 b). A visual assessment of Figure 3 b) shows no distortion of the diffraction pattern. To quantitatively analyze the remaining tilt-induced diffraction shift, we subtracted the COM of the untilted diffraction pattern from the COMs of the tilted diffraction patterns. The result is plotted as a function of the azimuth angle in Figure 3 c), revealing an RMS tilt-induced diffraction shift of  $\sim 4 \mu\text{rad}$ , corresponding to  $\sim 1/4$  of a pixel.

The influence of tilt-induced beam shift is analyzed by similar means with an untilted beam and 16 tilted beams as described in the previous paragraph. Figure 3 d) shows an ADF image of FIB deposited Pt:C acquired without a beam tilt and Figure 3 e) shows the sum of the ADF images acquired with the 16 tilted beams from the same region without tilt-induced beam shift calibration. Tilting the beam clearly leads to blurring of the summed image. When the same image is created with tilt-induced beam shift correction, as shown in Figure 3 f), the image shows much less blur. This is confirmed by a decrease of the RMS tilt-induced beam shift from  $\sim 4 \text{ nm}$  to  $\sim 1 \text{ nm}$ , determined by cross-correlation of the ADF images. Thus, after calibration, the resulting RMS tilt-induced beam shift is smaller than the probe size.

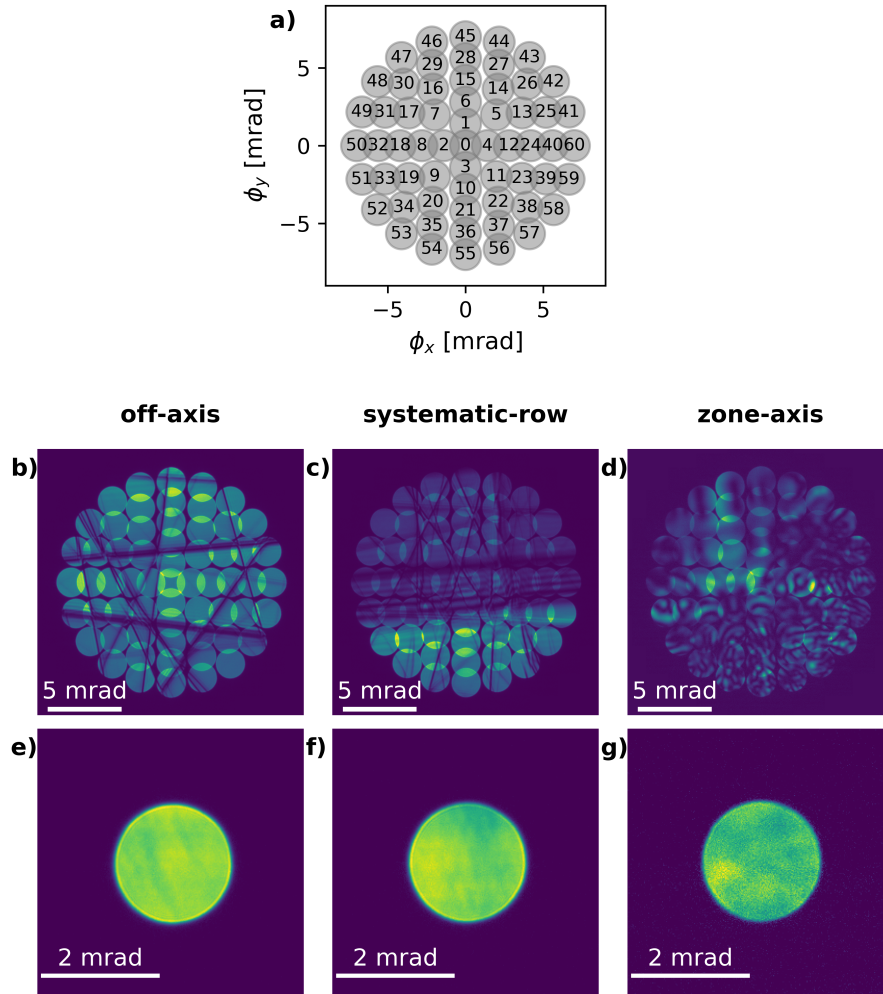


Figure 2: Beam tilt pattern and diffraction patterns: Figure a) shows the beam tilt pattern used throughout this work. Images b)-d) show the resulting vLACBED patterns for a field-free part of the sample on the GaAs side for three different sample orientations. The same diffraction patterns used for creating the vLACBED patterns are shown as averaged diffraction patterns in e)-g).

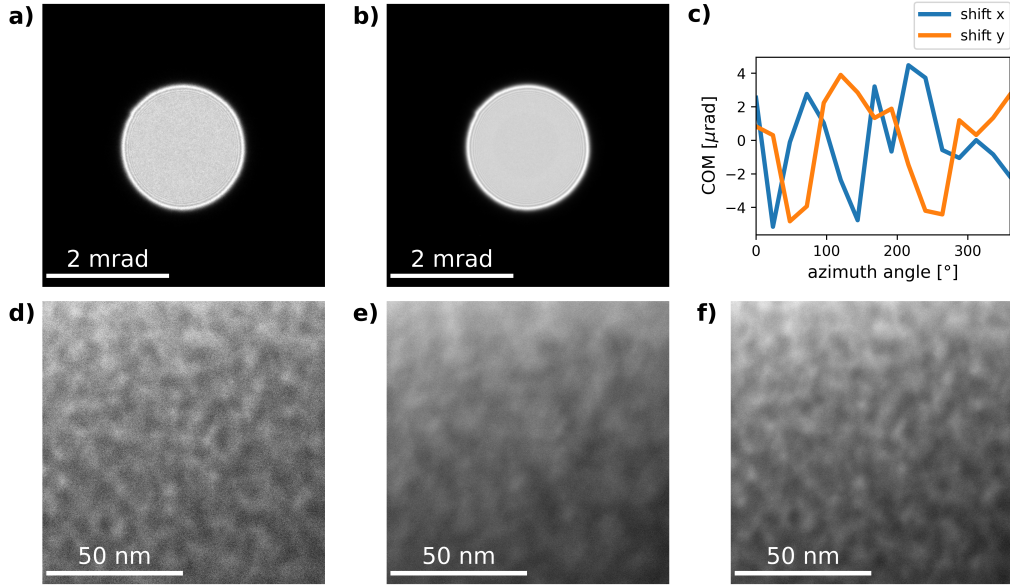


Figure 3: Calibrations of beam tilt and tilt-induced beam shift: **a)** shows a diffraction pattern acquired in vacuum without beam tilt. **b)** shows the sum of 16 diffraction patterns tilted along a circle with a radius of 7 mrad, under the same conditions as in **a)**. **c)** shows the change in COM of the 16 diffraction patterns of **b)** relative to the COM of the diffraction pattern of **a)** as a function of azimuth angle. **d)** shows an ADF image of FIB-deposited Pt particles acquired without beam tilt. **e)** shows the sum of 16 ADF images acquired with beam tilts along a circle with a radius of 7 mrad from the same region without tilt-induced beam shift correction. Figure **f)** shows the same image as **e)**, but with tilt-induced beam shift correction.

### 3.2 Evaluating MRSTEM data

Sequential tilting 4D-STEM provides more opportunities to evaluate the quality of MRSTEM data than conventional methods. This is evident when comparing the vLACBED pattern in Figure 2 **b)-d)** and the averaged diffraction pattern in Figure 2 **e)-g)**, which originate from the same data. For instance, the HOLZ lines and Bragg deficiency lines in the vLACBED pattern can be used to determine the sample orientation dependent on the scan position from sequential tilted 4D-STEM data. This information can then be used to optimize MRSTEM data processing.

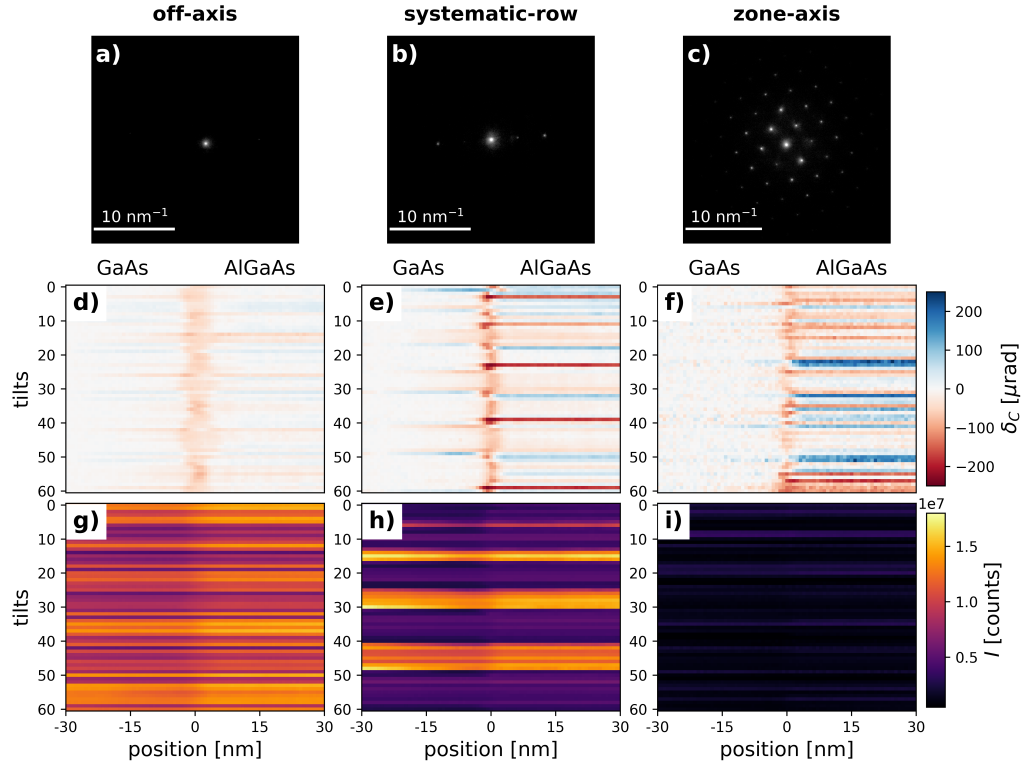


Figure 4: Residual COM and total intensity of the acquired diffraction patterns for different sample orientations: Images **a)**-**c)** show the SAED patterns for the off-axis, systematic-row and zone-axis orientation. Images **d)**-**f)** show the corresponding COM for each beam tilt and scan position, calculated by subtracting the average COM from a field-free region (-30 nm to -20 nm). Images **g)**-**i)** show the total intensity of the acquired diffraction patterns for each beam tilt and scan position. The GaAs/AlGaAs interface is located at 0 nm.

Here, we evaluate the quality of the data for three different sample orientations: off-axis, systematic-row, and zone-axis. The zone-axis orientation refers to a [110] orientation of the lamella. The systematic-row orientation includes an  $8.5^\circ$  rotation around the interface normal with respect to the zone-axis orientation. The off-axis orientation adds another  $0.9^\circ$  rotation parallel to the interface normal. Thus, we expect the off-axis orientation to have the least dynamic diffraction conditions, but also an interface blur of about 5 nm. The corresponding selected area electron diffraction (SAED) patterns are shown in Figure 4 **a-c**).

For each sample orientation, we acquire sequential tilting 4D-STEM line scans across the AlGaAs/GaAs interface. We measure and correct the drift using ADF reference images taken after each sequential scan. From the drift-corrected MRSTEM data, we calculate the COM for every beam tilt and position. To correct the data for descans, we apply the same processing to an MRSTEM vacuum reference and subtract the resulting reference COM from the measurement's COM. Furthermore, we rotate the COM vector to account for the difference in rotation between the sample and detector coordinate systems. For the following steps, we only use the COM perpendicular to the interface, as no field is expected to be parallel to the interface and no COM shift is observed in this direction. By subtracting the mean COM of a field-free region for each beam tilt, we obtain position-dependent COM changes relative to the field-free reference.

$$\delta_C(\mathbf{r}, \mathbf{K}) = \langle \mathbf{p} \rangle(\mathbf{r}, \mathbf{K}) - \overline{\langle \mathbf{p} \rangle}(\mathbf{K}) \quad (1)$$

where  $\langle \mathbf{p} \rangle(\mathbf{r}, \mathbf{K})$  is the COM for a given scan position  $\mathbf{r}$  and beam tilt  $\mathbf{K}$  and  $\overline{\langle \mathbf{p} \rangle}(\mathbf{K})$  is the mean COM from a field free region. Thus, the magnitude of  $\delta_C$  measures how strongly the COM changes, either due to local fields or local changes of the diffraction condition.  $\delta_C$  is plotted for the three sample orientations in Figure 4 **d-f**), where  $\overline{\langle \mathbf{p} \rangle}(\mathbf{K})$  was averaged between -20 nm and -30 nm on the GaAs side. As expected, the  $\delta_C$  maps show small variations on the GaAs side of the junction and the smallest variations for off-axis orientation. The other two orientations exhibit a significant increase in  $\delta_C$  on the entire AlGaAs side of the junction, indicating that a change in diffraction conditions causes the COM shift. For the systematic-row orientation, only a few beam tilts show strong COM shifts on the AlGaAs side. For the zone-axis orientation, most beam tilts show strong COM shifts on the AlGaAs side. This suggests that, in the systematic-row orientation, certain beam tilts remain relatively unaffected by changes in diffraction conditions. In contrast,

close to the zone-axis, almost all beam tilts are significantly impacted by these changes. We will use this insight to optimize the data processing in the following section.

Furthermore, we can plot the total intensity of the acquired diffraction patterns as a function of scan position and beam tilt, i.e., tilt-dependent virtual bright field images, as shown in Figure 4 **g-i**). When we compare the intensities to the change in the COM across the interface, we observe a correlation between low intensities and significant COM changes for off-axis and systematic-row orientations. This is to be expected, as the acquired diffraction patterns only contain the direct beam, and more dynamic diffraction conditions result in lower intensity in the direct beam for off-axis and systematic-row orientations. For zone-axis orientation, no clear correlation is observed between the COM change across the interface and the intensity.

### 3.3 Potential mapping

In general, we can calculate the tilt averaged COM

$$\overline{\langle \mathbf{p} \rangle}(\mathbf{r}) = \frac{\sum_{\mathbf{K}=0}^N a(\mathbf{r}, \mathbf{K}) \langle \mathbf{p} \rangle(\mathbf{r}, \mathbf{K})}{\sum_{\mathbf{K}=0}^N a(\mathbf{r}, \mathbf{K})} \quad (2)$$

where  $a(\mathbf{r}, \mathbf{K})$  is a tilt and position dependent weighting factor.

The simplest approach is to set all  $a(\mathbf{r}, \mathbf{K})$  to 1, which is different from the conventional precession MRSTEM approach, where the diffraction patterns are first averaged and then the COM is calculated. Thus, conventional precession MRSTEM implicitly weights the tilted diffraction patterns by their intensity. We can reproduce this weighting by setting  $a(\mathbf{r}, \mathbf{K})$  to the total intensity of the respective diffraction pattern. Furthermore, we can construct other weights using a priori knowledge about the sample. We can design weights that are high when the COM residuals between field-free parts on opposite sides of the junction are small.

$$a(\mathbf{K}) = \frac{1}{|\overline{\langle \mathbf{p} \rangle}(\mathbf{K})_{\text{GaAs}} - \overline{\langle \mathbf{p} \rangle}(\mathbf{K})_{\text{AlGaAs}}| + \epsilon} \quad (3)$$

where  $\overline{\langle \mathbf{p} \rangle}(\mathbf{K})_{\text{GaAs}}$  and  $\overline{\langle \mathbf{p} \rangle}(\mathbf{K})_{\text{AlGaAs}}$  are averaged over field free regions on the GaAs and AlGaAs side respectively and  $\epsilon$  is a small regularization constant to avoid diverging weights.

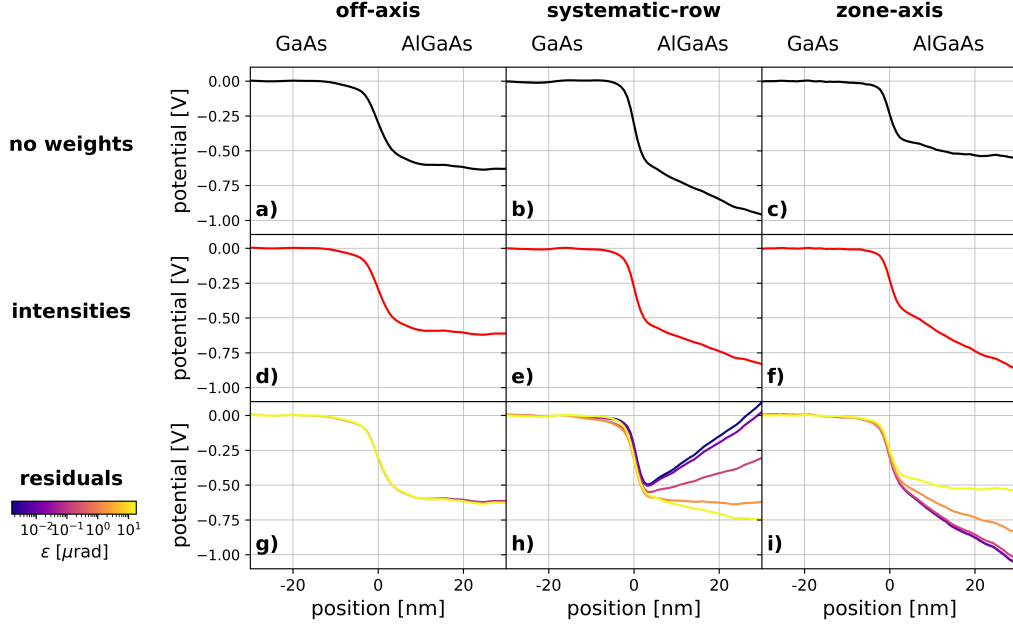


Figure 5: Potential distributions across the AlGaAs/GaAs junction for different sample orientations and post-processing treatments: **a)-c)** show the potential distributions across the interface for different sample orientations when the COM is first calculated for every beam tilt and then averaged. **d)-f)** show potential distributions obtained from the same data, but with the COMs weighted by their intensities. **g)-i)** show potential distributions obtained using residual COMs for weighting as a function of the regularization parameter  $\epsilon$ . The GaAs/AlGaAs interface is located at 0 nm.

We use the resulting tilt-averaged COM values to calculate the electric field in the sample. We do this by using the interaction constant and lamella thickness while assuming the field is constant along the electron beam direction. By integrating the electric field along the scan direction, we obtain the potential distribution across the interface. Figure 5 summarizes and compares the potential distributions across the AlGaAs/GaAs interface for different sample orientations and analysis strategies.

Beginning the discussion regarding the off-axis orientation shown in Figure 5 **a)**, **d)** and **g)**, we observe an excellent agreement between the measured and expected potentials. The potential drops at the interface and remains constant on both sides of the junction. This is true for all types of applied

data analysis. In general, MRSTEM measurements appear quite reliable under these weak diffraction conditions.

The situation is different for the systematic-row orientation, shown in Figure 5 b), e) and h). In this case, there is a linear decrease in the measured potential on the field-free AlGaAs side without weights, indicating that a change in the diffraction condition causes an offset in the COM. The intensity-weighted potential exhibits slightly better behavior than the potential without weights, which can be understood intuitively by considering the intensity dependence of the direct diffraction disc. In this orientation, stronger diffraction results in more intensity being transferred to the diffracted discs, resulting in less intensity in the direct disc. Thus, intensity is an effective weight for suppressing contributions from beam tilts with strong diffraction under these conditions. Moreover, constructing the weights from the residual COM with the proper choice of  $\epsilon$ , in this case  $\epsilon \approx 1 \mu\text{rad}$ , yields a significantly improved result. Since the optimally processed potential distribution almost exactly matches the corresponding off-axis potential distributions, it is evident that proper data processing mitigates the impact of dynamic diffraction on the MRSTEM results.

The behavior is different for the zone-axis orientation shown in Figure 5 c), f) and i). No weighting yields better results than intensity weighting. This is because the correlation between dynamic diffraction artifacts in the MRSTEM data and the intensity of the direct disc is absent under strongly dynamic diffraction conditions. Thus, the improvement by tilt averaging is solely due to incoherently averaging more diffraction patterns. When weights are calculated based on the residual COM, the best result is obtained with a large  $\epsilon$  value. This leads to equal weights for all beam tilts, resulting in the same outcome as without weights. This indicates that all beam tilts are strongly affected by dynamic diffraction for this sample orientation, and excluding data from the averaging process only worsens the MRSTEM results.

## 4 Conclusion

In this work, we presented an implementation of sequential tilting 4D-STEM. Our implementation enables robust alignment of beam tilt and detilt, yielding a residual diffraction shift of  $\sim 4 \mu\text{rad}$  and a tilt-induced beam shift of  $\sim 1 \text{ nm}$ , without requiring additional hardware. Furthermore, we tested sev-

eral strategies for using the additional information obtained through sequential tilting 4D-STEM to improve the reliability of MRSTEM results under different diffraction conditions. In doing so, we identified different regimes of dynamic diffraction by accessing MRSTEM data from individual beam tilts. Sequential tilting MRSTEM generally yields good results for weak diffraction conditions. For medium and strong diffraction conditions, we improved the sequential tilting MRSTEM results through appropriate data processing, which are inherently inaccessible for previous MRSTEM techniques. This demonstrates the benefits of sequential tilting 4D-STEM for the reliability and accuracy of MRSTEM measurements.

We are convinced that using direct electron detectors, improving beam tilt patterns, and optimizing data post-processing will further improve the results and will enable measurements on more complex samples using sequential tilting 4D-STEM. In the future, combining sequential tilting 4D-STEM with other STEM-based electric characterization techniques, such as STEM EBIC [40] and in situ biasing, will enable reliable, quantitative, and comprehensive measurements of junction properties of real devices on the nanometer scale. In addition, we expect that sequential tilting 4D-STEM will help to develop strategies to suppress dynamic diffraction effects in other applications like domain, phase, or strain mapping as well.

## CRediT authorship contribution statement

**Christoph Flathmann:** Conceptualization; Data curation; Formal analysis; Investigation; Methodology; Software; Validation; Visualization; Writing – original draft; Writing – review & editing. **Ulrich Ross:** Investigation; Writing – review & editing. **Jürgen Belz:** Resources; Writing – review & editing. **Andreas Beyer:** Resources; Writing – review & editing. **Kerstin Volz:** Funding acquisition; Resources; Writing – review & editing. **Michael Seibt:** Funding acquisition; Supervision; Writing – original draft; Writing – review & editing. **Tobias Meyer:** Conceptualization; Data curation; Methodology; Software; Project administration; Writing – original draft; Writing – review & editing.

## Acknowledgements

This work was supported by the Deutsche Forschungsgemeinschaft (DFG, German Research Foundation) – 217133147/SFB 1073, projects B02 and Z02. The use of equipment of the “Collaborative Laboratory and User Facility for Electron Microscopy” (CLUE, Göttingen) is gratefully acknowledged.

## References

- [1] B. J. Baliga, Fundamentals of power semiconductor devices, Springer Science & Business Media, 2010.
- [2] P. Würfel, U. Würfel, Physics of solar cells: from basic principles to advanced concepts, John Wiley & Sons, 2016.
- [3] K. Yamamoto, Y. Iriyama, T. Asaka, T. Hirayama, H. Fujita, C. A. Fisher, K. Nonaka, Y. Sugita, Z. Ogumi, Dynamic visualization of the electric potential in an all-solid-state rechargeable lithium battery, *Angew. Chem* 49 (26) (2010) 4414–4417.
- [4] J. Haruyama, K. Sodeyama, L. Han, K. Takada, Y. Tateyama, Space-charge layer effect at interface between oxide cathode and sulfide electrolyte in all-solid-state lithium-ion battery, *Chemistry of Materials* 26 (14) (2014) 4248–4255.
- [5] L. Wang, R. Xie, B. Chen, X. Yu, J. Ma, C. Li, Z. Hu, X. Sun, C. Xu, S. Dong, et al., In-situ visualization of the space-charge-layer effect on interfacial lithium-ion transport in all-solid-state batteries, *Nature Communications* 11 (1) (2020) 5889.
- [6] A. Tonomura, Applications of electron holography, *Reviews of modern physics* 59 (3) (1987) 639.
- [7] H. Lichte, P. Formanek, A. Lenk, M. Linck, C. Matzeck, M. Lehmann, P. Simon, Electron holography: Applications to materials questions, *Annu. Rev. Mater. Res.* 37 (1) (2007) 539–588.
- [8] S. Frabboni, G. Matteucci, G. Pozzi, M. Vanzi, Electron holographic observations of the electrostatic field associated with thin reverse-biased p-n junctions, *Physical review letters* 55 (20) (1985) 2196.

- [9] W. Rau, P. Schwander, F. Baumann, W. Höppner, A. Ourmazd, Two-dimensional mapping of the electrostatic potential in transistors by electron holography, *Physical Review Letters* 82 (12) (1999) 2614.
- [10] A. Twitchett, R. Dunin-Borkowski, P. Midgley, Quantitative electron holography of biased semiconductor devices, *Physical review letters* 88 (23) (2002) 238302.
- [11] D. Cooper, Off-axis electron holography for the measurement of active dopants in silicon semiconductor devices, *Journal of Physics D: Applied Physics* 49 (47) (2016) 474001.
- [12] H. Sasaki, S. Otomo, R. Minato, K. Yamamoto, T. Hirayama, Direct observation of dopant distribution in GaAs compound semiconductors using phase-shifting electron holography and Lorentz microscopy, *Journal of Electron Microscopy* 63 (3) (2014) 235–242.
- [13] S. Anada, K. Yamamoto, H. Sasaki, N. Shibata, M. Matsumoto, Y. Hori, K. Kinugawa, A. Imamura, T. Hirayama, Accurate measurement of electric potentials in biased GaAs compound semiconductors by phase-shifting electron holography, *Microscopy* 68 (2) (2019) 159–166.
- [14] D. Cooper, V. Fan Arcara, B. Damilano, L. Amichi, A. Mavel, N. Rochat, G. Feuillet, A. Courville, S. Vézian, J. Duboz, Mapping of the electrostatic potentials in MOCVD and hybrid GaN tunnel junctions for InGaN/GaN blue emitting light emitting diodes by off-axis electron holography correlated with structural, chemical, and optoelectronic characterization, *Journal of Applied Physics* 130 (2) (2021).
- [15] D. Cooper, C. Licitra, Y. Boussadi, B. Ben-Bakir, B. Masenelli, Mapping of the Electrostatic Potentials in a Fully Processed Led Device with nm-Scale Resolution by In Situ off-Axis Electron Holography, *Small Methods* 7 (9) (2023) 2300537.
- [16] K. Müller, F. F. Krause, A. Béché, M. Schowalter, V. Galioit, S. Löffler, J. Verbeeck, J. Zweck, P. Schattschneider, A. Rosenauer, Atomic electric fields revealed by a quantum mechanical approach to electron picodiffraction, *Nature communications* 5 (1) (2014) 5653.

- [17] F. Winkler, J. Barthel, R. E. Dunin-Borkowski, K. Müller-Caspary, Direct measurement of electrostatic potentials at the atomic scale: A conceptual comparison between electron holography and scanning transmission electron microscopy, *Ultramicroscopy* 210 (2020) 112926.
- [18] N. Shibata, S. D. Findlay, H. Sasaki, T. Matsumoto, H. Sawada, Y. Kohno, S. Otomo, R. Minato, Y. Ikuhara, Imaging of built-in electric field at a pn junction by scanning transmission electron microscopy, *Scientific reports* 5 (1) (2015) 10040.
- [19] T. Seki, G. Sánchez-Santolino, R. Ishikawa, S. D. Findlay, Y. Ikuhara, N. Shibata, Quantitative electric field mapping in thin specimens using a segmented detector: Revisiting the transfer function for differential phase contrast, *Ultramicroscopy* 182 (2017) 258–263.
- [20] L. Clark, H. Brown, D. Paganin, M. Morgan, T. Matsumoto, N. Shibata, T. Petersen, S. Findlay, Probing the limits of the rigid-intensity-shift model in differential-phase-contrast scanning transmission electron microscopy, *Physical Review A* 97 (4) (2018) 043843.
- [21] B. Haas, J.-L. Rouviere, V. Boureau, R. Berthier, D. Cooper, Direct comparison of off-axis holography and differential phase contrast for the mapping of electric fields in semiconductors by transmission electron microscopy., *Ultramicroscopy* 198 (2019) 58–72.
- [22] S. Toyama, T. Seki, S. Anada, H. Sasaki, K. Yamamoto, Y. Ikuhara, N. Shibata, Quantitative electric field mapping of ap–n junction by DPC STEM, *Ultramicroscopy* 216 (2020) 113033.
- [23] L. Bruas, V. Boureau, A. Conlan, S. Martinie, J.-L. Rouviere, D. Cooper, Improved measurement of electric fields by nanobeam precession electron diffraction, *Journal of Applied Physics* 127 (20) (2020).
- [24] A. Beyer, M. S. Munde, S. Firoozabadi, D. Heimes, T. Grieb, A. Rosenauer, K. Müller-Caspary, K. Volz, Quantitative characterization of nanometer-scale electric fields via momentum-resolved STEM, *Nano letters* 21 (5) (2021) 2018–2025.
- [25] B. C. da Silva, Z. Sadre Momtaz, E. Monroy, H. Okuno, J.-L. Rouviere, D. Cooper, M. I. Den Hertog, Assessment of Active Dopants and p–

- n Junction Abruptness Using In Situ Biased 4D-STEM, *Nano Letters* 22 (23) (2022) 9544–9550.
- [26] V. S. Chejarla, S. Ahmed, J. Belz, J. Scheunert, A. Beyer, K. Volz, Measuring Spatially-Resolved Potential Drops at Semiconductor Hetero-Interfaces Using 4D-STEM, *Small Methods* 7 (9) (2023) 2300453.
- [27] C. Mahr, T. Grieb, F. F. Krause, M. Schowalter, A. Rosenauer, Towards the interpretation of a shift of the central beam in nano-beam electron diffraction as a change in mean inner potential, *Ultramicroscopy* 236 (2022) 113503.
- [28] D. Heimes, V. S. Chejarla, S. Ahmed, F. Hüppe, A. Beyer, K. Volz, Impact of beam size and diffraction effects in the measurement of long-range electric fields in crystalline samples via 4DSTEM, *Ultramicroscopy* 253 (2023) 113821.
- [29] T. Mawson, A. Nakamura, T. Petersen, N. Shibata, H. Sasaki, D. Paganin, M. Morgan, S. Findlay, Suppressing dynamical diffraction artefacts in differential phase contrast scanning transmission electron microscopy of long-range electromagnetic fields via precession, *Ultramicroscopy* 219 (2020) 113097.
- [30] P. A. Midgley, A. S. Eggeman, Precession electron diffraction—a topical review, *IUCrJ* 2 (1) (2015) 126–136.
- [31] D. Cooper, L. Bruas, M. Bryan, V. Boureau, Measuring electrical properties in semiconductor devices by pixelated STEM and off-axis electron holography (or convergent beams vs. plane waves)., *Micron* 179 (2024) 103594.
- [32] Y. O. Murakami, T. Seki, A. Kinoshita, T. Shoji, Y. Ikuhara, N. Shibata, Magnetic-structure imaging in polycrystalline materials by specimen-tilt series averaged DPC STEM, *Microscopy* 69 (5) (2020) 312–320.
- [33] Y. Kohno, A. Nakamura, S. Morishita, N. Shibata, Development of tilt-scan system for differential phase contrast scanning transmission electron microscopy, *Microscopy* 71 (2) (2022) 111–116.

- [34] S. Toyama, T. Seki, Y. Kanitani, Y. Kudo, S. Tomiya, Y. Ikuhara, N. Shibata, Quantitative electric field mapping in semiconductor heterostructures via tilt-scan averaged DPC STEM, *Ultramicroscopy* 238 (2022) 113538.
- [35] S. Toyama, T. Seki, Y. Kanitani, Y. Kudo, S. Tomiya, Y. Ikuhara, N. Shibata, Real-space observation of a two-dimensional electron gas at semiconductor heterointerfaces, *Nature Nanotechnology* 18 (5) (2023) 521–528.
- [36] S. Toyama, T. Seki, Y. Kohno, Y. O. Murakami, Y. Ikuhara, N. Shibata, Nanoscale electromagnetic field imaging by advanced differential phase-contrast STEM, *Nature Reviews Electrical Engineering* 2 (1) (2025) 27–41.
- [37] G. Nordahl, L. Jones, E. F. Christiansen, K. A. Hunnestad, M. Nord, Correcting for probe wandering by precession path segmentation, *Ultramicroscopy* 248 (2023) 113715.
- [38] K. Iakoubovskii, K. Mitsuishi, Y. Nakayama, K. Furuya, Thickness measurements with electron energy loss spectroscopy, *Microscopy research and technique* 71 (8) (2008) 626–631.
- [39] T. Meyer, Structural and electronic investigation of strongly correlated transition metal oxide perovskite thin films and interfaces using in-situ transmission electron microscopy, Ph.D. thesis, Dissertation, Göttingen, Georg-August Universität, 2020 (2021).
- [40] T. Meyer, D. A. Ehrlich, P. Pichler, V. Titova, C. Flathmann, J. Schmidt, M. Seibt, Tracing the boron diffusion into a textured silicon solar cell by combining boron diffusion simulation with experimental and simulated scanning transmission electron beam induced current, *arXiv preprint arXiv:2109.00586* (2021).